A Fast Multigrid Method for Solving the Nonlinear Ship Wave Problem with a Free Surface

J. Farmer, L. Martinelli
A. Jameson
Department of Mechanical and Aerospace Engineering
Princeton University
Princeton, NJ. 08544

6th International Conference on Numerical Ship Hydrodynamics
Iowa City, Iowa, 2-5 August 1993.

A Fast Multigrid Method for Solving the Nonlinear Ship Wave Problem with a Free Surface

J. Farmer*, L. Martinelli† and A. Jameson‡
Department of Mechanical and Aerospace Engineering
Princeton University
Princeton, NJ. 08544

[1]

Abstract

This paper presents a finite volume method for the solution of the three dimensional, nonlinear ship wave problem. The method can be used to obtain both Euler and Navier-Stokes solutions of the flow field and the *a priori* unknown free surface location by coupling the free surface kinematic and dynamic equations with the equations of motion for the bulk flow. The evolution of the free surface boundary condition is linked to the evolution of the bulk flow via a novel iteration strategy that allows temporary leakage of mass through the surface before the solution is converged. The method of artificial compressibility is used to enforce the incompressibility constraint for the bulk flow. A multigrid algorithm is used to accelerate convergence to a steady state. The two-layer eddy viscosity formulation of Baldwin and Lomax is used to model turbulence. The scheme is validated by comparing the numerical results with experimental results for the Wigley parabolic hull and the Series 60, $C_b = 0.6$ hull. Waterline profiles from bow to stern are in excellent agreement with experiment. The computed wave drag compares favorably with experiment. Overall, the present method proves to be accurate and efficient.

[1]Paper presented at the 6th International Conference on Numerical Ship Hydrodynamics, Iowa City, Iowa, 2-5 August 1993. To appear in the published conference proceedings.
* Research Associate.
† Research Staff Member.
‡ Professor.

1 Introduction

It is well established that a complex interaction exists between the viscous boundary layer and wake of a ship hull and the resulting wave pattern [1, 2]. The existence of two similarity parameters, the Froude number (Fr) and the Reynolds number (Re), which do not scale identically between model and full scale hulls, make it difficult to predict the viscous effect on the wave and total drag through model testing. The ship designer may thus resort to numerical simulation, and a great deal of effort has been devoted toward developing numerical tools capable of simulating the flow field about a translating ship. Some of these tools have met with success in capturing the salient features of the flow field, including the difficult-to-model stern region of ship hulls. However, many of the computational methods developed to date, especially those that include viscous effects and a moving free surface, tend to be very complicated and expensive. Thus, the focus of this work is the development of a fast and robust means to compute either viscous or inviscid flow fields about surface piercing ship hulls, and to make comparisons with experimental data.

The method of Hino [3] is a widely used approach for solving incompressible flow problems. This method takes the divergence of the momentum equation and solves implicit equations at each time step for the pressure and velocity fields such that continuity is satisfied. The method is expensive both because of the need to solve implicit equations by an iterative method and because of the cost of calculating the divergence of the momentum equations in a curvilinear coordinate system. Hino uses a finite difference scheme expressed in body-fitted curvilinear coordinates to discretize the solution domain on and below

the free surface. The computational grid is not allowed to move with the free surface so an approximation must be employed to model the free surface boundary conditions. A Baldwin-Lomax turbulence model is used in conjunction with the wall function to model the viscous boundary layer. The scheme is first-order accurate in time and requires 10^4-plus global iterations to reach steady state for simple hull shapes.

The method of Miyata *et al.* (1987) [4] uses a similar velocity and pressure coupling procedure but now the grid is allowed to move with the free surface, providing a more exact treatment of the free surface boundary conditions. A sub-grid-scale turbulence model is employed and computations performed for Reynolds numbers up to 10^5. As with Hino's method, the time-accurate formulation necessitates several thousand time steps to reach steady state solutions. In a later paper, Miyata *et al.* (1992) [5] present a finite volume approach that substantially improves the computed results over those obtained using the finite difference approach. Simulations using Reynolds numbers up to 10^6 were made and more complicated hull shapes examined. The method still requires many thousands of time steps to achieve steady state solutions.

The interactive approach of Tahara *et al.* [6] uses a field method based on the finite-analytic method used by Chen *et al.* [7] for the viscous region, and a surface singularity method based on the "SPLASH" panel method of Rosen [8] for the inviscid outer domain. The method iterates between the inviscid and viscous regions by adjusting the small-domain panel distribution to allow for the boundary layer displacement thickness determined from the large-domain solution. The free surface boundary conditions are linearized and applied at the mean water elevation surface. Results of this approach appear to be quite promising for the Wigley hull, and a substantial savings in required computational cost is realized over the large-domain approaches of Hino and Miyata.

In this work, a field method is adopted for the entire flow domain like Hino and Miyata. However, the incompressibility constraint is enforced through the method of *artificial compressibility*, rather than the velocity-pressure coupling method. The method of artificial compressibility was originally proposed by Chorin [9] in 1967 to solve viscous flows. Since then, Rizzi and Eriksson [10] have applied it to rotational inviscid flow, Dreyer [11] has applied it to low speed two dimensional airfoils and Kodama [12] has applied it to ship hull forms with a symmetric free surface. In addition, Turkel [13] has investigated more sophisticated preconditioners than those originally proposed by Chorin. The basic idea behind artificial compressibility is to introduce a pseudotemporal equation for the pressure through the continuity equation. Use of this pressure equation, rather than the velocity-pressure coupling procedure described in references [3] - [7], renders the new set of equations well conditioned for numerical computation along the same lines as those used to calculate compressible flow about complete aircraft [14, 15]. When combined with multigrid acceleration procedures [16, 17, 18] it proves to be particularly effective. Converged solutions of incompressible flows over three dimensional isolated wings are obtained in 25-50 cycles.

The general objective of this work is to build on these ideas to develop a more efficient method to predict free surface wave phenomena, for both inviscid and viscous flows. The viscous solution method introduced in this work is an extension of the inviscid method presented in reference [19, 20]. The nonlinear free surface boundary condition is satisfied by an iterative procedure in which the grid is moved with the free surface. Comparisons of numerical predictions with experimental data, for the Wigley hull and Series 60, $C_b = 0.6$ ship hull, show encouraging results for both waterline profiles and wave drag. Furthermore, it appears that this approach yields a substantial savings in the computational resources required for the simulations.

2 Mathematical Model

Figure 1 shows the reference frame and ship location used in this work. A right-handed coordinate system $Oxyz$, with the origin fixed at midship on the mean free surface is established. The z direction is positive upwards, y is positive towards the starboard side and x is positive in the aft direction. The free stream velocity vector is parallel to the x axis and points in the same direction. The ship hull pierces the uniform flow and is held fixed in place, ie. the ship is not allowed to sink (translate in z direction) or trim (rotate in $x - z$ plane).

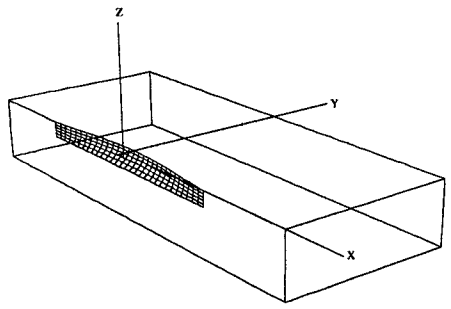

Figure 1: Reference Frame and Ship Location

2.1 Bulk Flow

For a viscous incompressible fluid moving under the influence of gravity, the continuity equation and the Reynolds averaged Navier-Stokes equations may be put in the form [3],

$$u_x + v_y + w_z = 0 \tag{1}$$

$$\begin{aligned} u_t + uu_x + vu_y + wu_z = \\ -\psi_x + \left(Re^{-1} + \nu_t\right)\left(\nabla^2 u\right) \end{aligned}$$

$$\begin{aligned} v_t + uv_x + vv_y + wv_z = \\ -\psi_y + \left(Re^{-1} + \nu_t\right)\left(\nabla^2 v\right) \end{aligned} \tag{2}$$

$$\begin{aligned} w_t + uw_x + vw_y + ww_z = \\ -\psi_z + \left(Re^{-1} + \nu_t\right)\left(\nabla^2 w\right). \end{aligned}$$

Here, $u = u(x,y,z,t)$, $v = v(x,y,z,t)$ and $w = w(x,y,z,t)$ are the mean total velocity components in the x, y and z directions. All lengths and velocities are nondimensionalized by the ship length L and the free stream velocity U, respectively. The pressure ψ is the static pressure p minus the hydrostatic component $-zFr^{-2}$ and may be expressed as $\psi = p + zFr^{-2}$, where $Fr = \frac{U}{\sqrt{gL}}$ is the Froude number. The pressure variable ψ is nondimensionalized by ρU^2. The Reynolds number Re is defined by $Re = \frac{UL}{\nu}$ where ν is the kinematic viscosity of water and is constant. ν_t is the dimensionless turbulent eddy viscosity, computed locally using the Baldwin-Lomax turbulence model. This set of equations shall be solved subject to the following boundary conditions.

2.2 Boundary Conditions

2.2.1 Free Surface

When the effects of surface tension and viscosity are neglected, the boundary condition on the free surface consists of two equations. The first, the dynamic condition, states that the pressure acting on the free surface is constant. The second, the kinematic condition, states that the free surface is a material surface: once a fluid particle is on the free surface, it forever remains on the surface. The dynamic and kinematic boundary conditions may be expressed as

$$p = constant$$

$$\frac{d\beta}{dt} = w = \beta_t + u\beta_x + v\beta_y \tag{3}$$

where $z = \beta(x,y,t)$ is the free surface location. Equation 3 only permits solutions where β is single valued. Consequently, it does not allow for the breaking of bow waves which can often be observed with cruiser type hulls. Breaking waves are difficult to treat numerically and are not considered in this work.

2.2.2 Hull and Farfield

The remaining boundaries consist of the ship hull, the boundaries which comprise the symmetry portions of the meridian plane and the far field of the computational domain. On the ship hull, the condition is that of no-slip and is stated simply by

$$u = v = w = 0.$$

On the symmetry plane (that portion of the (x,z) plane excluding the ship hull) derivatives in the y direction as well as the v component of velocity are set to zero. The upstream plane has $u = U$ and $\psi = 0$ ($p = -zFr^{-2}$) with the v and w velocity components set to zero. Similar conditions hold on the bottom plane which is assumed to represent infinitely deep water where no disturbances are felt. One-sided differences are used to update the flow variables on the starboard plane. A radiation condition should be imposed on the outflow domain to allow the wave disturbance to pass out of the computational domain. Although fairly sophisticated formulations may be devised to represent the radiation condition, simple extrapolations proved to be sufficient in this work.

2.3 Turbulence Model

To model turbulence in the flow field the laminar viscosity is replaced by

$$\mu = \mu_l + \mu_t$$

where the turbulent viscosity μ_t is computed using the algebraic model of Baldwin and Lomax [22]. The Baldwin-Lomax model is an algebraic scheme that makes use of a two-layer, isotropic eddy viscosity formulation. In this model the turbulent viscosity is evaluated using

$$\mu_t = \begin{cases} (\mu_t)_{inner} & y \leq y_{crossover} \\ (\mu_t)_{outer} & y > y_{crossover} \end{cases}$$

where y is the distance measured normal to the body surface and $y_{crossover}$ is the minimum value of y where both the inner and outer viscosities match. The inner viscosity follows the Prandtl-Van Driest formula,

$$(\mu_t)_{inner} = l^2|\omega|$$

where

$$l = ky\left[1 - exp(-y^+/A^+)\right]$$

is the turbulent length scale for the inner region, k and A^+ are model constants, $|\omega|$ is the vorticity magnitude and $y^+ = (\tau_w/\mu_w)y$ is the dimensionless distance to the wall in wall units.

In the outer region of the boundary layer, the turbulent viscosity is given by

$$(\mu_t)_{outer} = KC_{cp}F_{wake}F_{Kleb}$$

where K and C_{cp} are model constants, the function F_{wake} is

$$F_{wake} = min\left(y_{max}F_{max}, C_{wk}y_{max}U_{dif}^2/F_{max}\right)$$

and the function F_{Kleb} is

$$F_{Kleb} = \left[1 + 5.5\left(\frac{C_{Kleb}y}{y_{max}}\right)^6\right]^{-1}.$$

The quantities F_{max} and y_{max} are determined by the value and corresponding location, respectively, of the maximum of the function

$$F = y|\omega|\left[1 - exp(-y^+/A^+)\right].$$

The quantity U_{dif} is the difference between maximum and minimum velocity magnitudes in the profile and is expressed as

$$U_{dif} = (u^2 + v^2 + w^2)_{max}^{1/2} - (u^2 + v^2 + w^2)_{min}^{1/2}$$

C_{Kleb} and C_{wk} are additional model constants. Numerical values for the model constants used in the computations are listed here:

$$A^+ = 26,\ k = 0.4,\ K = 0.0168,$$

and

$$C_{cp} = 1.6,\ C_{wk} = 1.0,\ C_{Kleb} = 0.3.$$

3 Numerical Solution

The formulation of the numerical solution procedure is based on a finite volume method (FVM) for the bulk flow variables (u, v, w and ψ), coupled to a finite difference method for the free surface evolution variables (β and ψ). Alternative cell-centered and cell-vertex formulations may be used in finite volume schemes [16]. A cell-vertex formulation was preferred in this work because values of the flow variables are needed on the boundary to implement the free surface boundary condition. The bulk flow is solved subject to Dirichlet conditions for the free surface pressure, followed by a free surface update via the bulk flow solution (ie. constant values for the velocities in equation 3). Each formulation is explicit and uses local time stepping. Both multigrid and residual averaging techniques are used in the bulk flow to accelerate convergence.

3.1 Bulk Flow Solution

Following Chorin [9] and more recently Yang *et al.* [23], the governing set of incompressible flow equations may be written in vector form as

$$\mathbf{w}_{t^*} + (\mathbf{f} - \mathbf{f_v})_x + (\mathbf{g} - \mathbf{g_v})_y + (\mathbf{h} - \mathbf{h_v})_z = 0 \quad (4)$$

where the vector of dependent variables $\mathbf{w}$ and inviscid flux vectors $\mathbf{f}$, $\mathbf{g}$ and $\mathbf{h}$ are given by

$$\begin{aligned} \mathbf{w} &= [\psi,\ u,\ v,\ w]^T \\ \mathbf{f} &= \left[\Gamma^2 u,\ u^2 + \psi,\ uv,\ uw\right]^T \\ \mathbf{g} &= \left[\Gamma^2 v,\ vu,\ v^2 + \psi,\ vw\right]^T \\ \mathbf{h} &= \left[\Gamma^2 w,\ wu,\ wv,\ w^2 + \psi\right]^T. \end{aligned}$$

The viscous flux vectors $\mathbf{f_v}$, $\mathbf{g_v}$ and $\mathbf{h_v}$ are given by

$$\begin{aligned} \mathbf{f_v} &= [0,\ \tau_{xx},\ \tau_{xy},\ \tau_{xz}]^T \\ \mathbf{g_v} &= [0,\ \tau_{yx},\ \tau_{yy},\ \tau_{yz}]^T \\ \mathbf{h_v} &= [0,\ \tau_{zx},\ \tau_{zy},\ \tau_{zz}]^T \end{aligned}$$

where the viscous stress components are defined as

$$\begin{aligned}
\tau_{xx} &= (Re^{-1}+\nu_t)(2u_x - 2/3(u_x+v_y+w_z)) \\
\tau_{yy} &= (Re^{-1}+\nu_t)(2v_y - 2/3(u_x+v_y+w_z)) \\
\tau_{zz} &= (Re^{-1}+\nu_t)(2w_z - 2/3(u_x+v_y+w_z)) \\
\tau_{xy} &= (Re^{-1}+\nu_t)(u_y+v_x) \\
\tau_{yz} &= (Re^{-1}+\nu_t)(v_z+w_y) \\
\tau_{zx} &= (Re^{-1}+\nu_t)(w_x+u_z).
\end{aligned}$$

Γ is called the "artificial compressibility" parameter due to the analogy that may be drawn between the above equations and the equations of motion for a compressible fluid whose equation of state is given by [9]

$$\psi = \Gamma^2 \rho.$$

Thus, ρ is an artificial density and Γ may be referred to as an artificial sound speed. When the temporal derivatives tend to zero, the set of equations satisfy precisely the incompressible equations 2, with the consequence that the correct pressure may be established using the artificial compressibility formulation. The artificial compressibility parameter may be viewed as a device to create a well posed system of hyperbolic equations that are to be integrated to steady state along lines similar to the well established compressible flow FVM formulation [18]. In addition, the artificial compressibility parameter may be viewed as a relaxation parameter for the pressure iteration. Note that temporal derivatives are now denoted by t^* to indicate pseudo time; the artificial compressibility, as formulated in the present work, destroys time accuracy.

To demonstrate the effect of Γ on the above set of equations and to establish the hyperbolicity of the set, the convective part of equation 4 may be written in quasi-linear form to determine the eigenvalues [10]. The eigenvalues are found to be

$$\lambda_1 = U, \;\; \lambda_2 = U, \;\; \lambda_3 = U + a, \;\; \lambda_4 = U - a,$$

where

$$U = u\omega_x + v\omega_y + w\omega_z$$

and

$$a^2 = U^2 + \Gamma^2(\omega_x^2 + \omega_y^2 + \omega_z^2).$$

The wave number components ω_x, ω_y and ω_z are defined on $-\infty \leq \omega_x, \omega_y, \omega_z \leq +\infty$. Since the eigenvalues are clearly real for any value of ω_x, ω_y and ω_z, the system of equations 4 is hyperbolic.

The choice of Γ is crucial in determining convergence and stability properties of the numerical scheme. Typically, the convergence rate of the scheme is dictated by the slowest system waves and the stability of the scheme by the fastest. In the limit of large Γ the difference in wave speeds can be large. Although this situation would presumably lead to a more accurate solution through the "penalty effect" in the pressure equation, very small time steps would be required to ensure stability. Conversely, for small Γ, the difference in the maximum and minimum wave speeds may be significantly reduced, but at the expense of accuracy. Thus a compromise between the two extremes is required. Following the work of Dreyer [11], the choice for Γ is taken to be

$$\Gamma^2 = \gamma(u^2 + v^2 + w^2),$$

where γ is a constant of order unity. In regions of high velocity and low pressure where suction occurs, Γ is large to improve accuracy, and in regions of lower velocity, Γ is correspondingly reduced.

The choice of Γ also influences the outflow boundary condition, or radiation condition. If it can be demonstrated that all system eigenvalues are both real and positive, then downstream or outflow boundary points may be extrapolated from the interior upstream flow. Even though an examination of the eigenvalues reveals that this can never be the case, the condition can be approached by a judicious choice of Γ. If Γ is large, extrapolation fails because the flow has both downstream and upstream dependence. As Γ is reduced, the upstream dependence becomes more pronounced and the downstream is reduced. Eventually, the upstream dependence is sufficiently dominant to allow extrapolation. Hence, all outflow variables are updated using zero gradient extrapolation.

Following the general procedures for FVM, the governing equations may be integrated over an arbitrary volume Λ. Application of the divergence theorem on the convective and viscous flux term integrals yields

$$\begin{aligned}
&\frac{\partial}{\partial t^*}\int_\Lambda \mathbf{w}\, d\Lambda + \\
&\quad \int_{\partial\Lambda} (\mathbf{f}dS_x + \mathbf{g}dS_y + \mathbf{h}dS_z) - \\
&\quad \int_{\partial\Lambda} (\mathbf{f_v}dS_x + \mathbf{g_v}dS_y + \mathbf{h_v}dS_z) = 0 \quad (5)
\end{aligned}$$

where S_x, S_y and S_z are the projected areas in the x, y and z directions, respectively. The

computational domain is divided into hexahedral cells. Application of FVM to each of the computational cells results in the following system of ordinary differential equations,

$$\frac{d}{dt^*}(\Lambda_{ijk}\mathbf{w}) + C_{ijk} - V_{ijk} = 0.$$

The volume Λ_{ijk} is given by the summation of the eight cells surrounding node i,j,k. The convective flux $C_{ijk}(\mathbf{w})$ is defined as

$$C_{ijk}(\mathbf{w}) = \sum_{k=1}^{n} (\mathbf{f}S_x + \mathbf{g}S_y + \mathbf{h}S_z)_k \quad (6)$$

and the viscous flux $V_{ijk}(\mathbf{w})$ is defined as

$$V_{ijk}(\mathbf{w}) = \sum_{k=1}^{n} (\mathbf{f_V}S_x + \mathbf{g_V}S_y + \mathbf{h_V}S_z)_k \quad (7)$$

where the summation is over the n faces surrounding Λ_{ijk}.

The projected areas may be computed by taking the cross product of the two vectors joining opposite corners of each cell face in the physical coordinate system. They correspond to the grid metrics $J\xi_x$, $J\xi_y$, $J\xi_z$, etc. appearing in a transformation to a curvilinear coordinate system $\xi = \xi(x,y,z)$, $\eta = \eta(x,y,z)$ and $\zeta = \zeta(x,y,z)$ where J is the Jacobian of the transformation. The flow variables required in the flux evaluation may be averaged on each cell face through the four nodal values associated with each face. Evaluation of the flux terms in equations 6 and 7 may be performed directly, without direct differentiation and without the need to handle grid singularities in a special fashion.

3.1.1 Artificial Dissipation

This scheme reduces to a second order accurate, nondissipative central difference approximation to the bulk flow equations on sufficiently smooth grids. A central difference scheme permits odd-even decoupling at adjacent nodes which may lead to oscillatory solutions. To prevent this "unphysical" phenomena from occurring, a dissipation term is added to the system of equations such that the system now becomes

$$\frac{d}{dt^*}(\Lambda_{ijk}\mathbf{w}) + [C_{ijk}(\mathbf{w}) - V_{ijk}(\mathbf{w}) - D_{ijk}(\mathbf{w})] = 0. \quad (8)$$

For the present problem a third order background dissipation term is added. The dissipative term is constructed in such a manner that the conservation form of the system of equations is preserved. The dissipation has the form

$$D_{ijk}(\mathbf{w}) = D_\xi + D_\eta + D_\zeta \quad (9)$$

where

$$D_{\xi_{ijk}} = d_{\xi_{i+1,j,k}} - d_{\xi_{i,j,k}}$$

and

$$d_{\xi_{i,j,k}} = \alpha\delta_\xi^2(\mathbf{w}_{i+1,j,k} - \mathbf{w}_{i,j,k}). \quad (10)$$

Similar expressions may be written for the η and ζ directions with δ_ξ^2, δ_η^2 and δ_ζ^2 representing second difference central operators.

In equation 10, the dissipation coefficient α is a scaling factor proportional to the local wave speed, and renders equation 9 third order in truncation terms so as not to detract from the second order accuracy of the flux discretization. The actual form for the coefficient is based on the spectral radius of the system and is given in the ξ direction as

$$\alpha = \epsilon(J|\tilde{u}| + \Gamma(S_x^2 + S_y^2 + S_z^2)^{1/2})$$

where $\tilde{u}$ is the contravariant velocity component

$$\tilde{u} = u\xi_x + v\xi_y + w\xi_z.$$

Similar dissipation coefficients are used for the η and ζ components in equation 9. The ϵ term is used to manually adjust the amount of dissipation.

3.1.2 Viscous Discretization

The discretization for the viscous fluxes follows the guidelines originally proposed in [24, 25] for the simulation of two dimensional viscous flows. The components of the stress tensor are computed at the cell centers with the aid of Gauss' formula. The viscous fluxes are then computed by making use of an auxiliary cell bounded by the faces lying on the planes containing the centers of the cells surrounding a given vertex and the mid-lines of the cell faces. For example, the u_x term in τ_{xx} may be computed from

$$u_x\Lambda = \int_\Lambda u_x d\Lambda = \int_{\partial\Lambda} u d\partial\Lambda_x \approx \sum_{k=1}^{6} u_k S_{x_k}$$

where $k = 1,6$ are the six faces surrounding a particular cell, u_k is an average of the velocities from the nodes that define the kth face and S_{x_k} are the projected areas in the x direction corresponding to each face. Once the components of the complete stress tensor are computed at the

centroids of the cells then the same method of evaluation may be used to compute the viscous fluxes at the vertex through use of equation 7. For this purpose the control volume is now constructed by assembling $\frac{1}{8}$ fractions of each of the eight cells surrounding a particular vertex. The equivalent two dimensional control volume is sketched in the figure below. This discretiza-

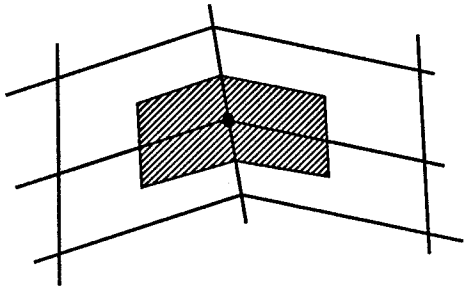

tion procedure is designed to minimize the error induced by a kink in the grid. It has proved to be accurate and efficient in applications to the solution of three dimensional compressible viscous flows [26, 27].

3.1.3 Time Integration

Equation 8 is integrated in time by an explicit multistage scheme. For each bulk flow time step, the grid, and thus Λ_{ijk}, is independent of time. Hence equation 8 can be written as

$$\frac{d\mathbf{w}_{ijk}}{dt^*} + R_{ijk}(\mathbf{w}) = 0, \qquad (11)$$

where the residual is defined as

$$R_{ijk}(\mathbf{w}) = C_{ijk}(\mathbf{w}) - V_{ijk}(\mathbf{w}) - D_{ijk}(\mathbf{w}),$$

and the cell volume Λ_{ijk} absorbed into the residual for clarity. If one analyzes a linear model problem corresponding to (11) by substituting a Fourier mode $\hat{w} = e^{ipx_j}$, the resulting Fourier symbol has an imaginary part proportional to the wave speed, and a negative real part proportional to the diffusion. Thus the time stepping scheme should have a stability region which contains a substantial interval of the negative real axis, as well as an interval along the imaginary axis. To achieve this it pays to treat the convective and dissipative terms in a distinct fashion. Thus the residual is split as

$$R_{ijk}(\mathbf{w}) = C_{ijk}(\mathbf{w}) + \mathcal{D}_{ijk}(\mathbf{w})$$

where $C_{ijk}(\mathbf{w})$ is the convective part and $\mathcal{D}_{ijk}(\mathbf{w}) = -(V_{ijk} + D_{ijk})$ the dissipative part. Denote the time level $n\Delta t$ by a superscript n, and drop the subscript for clarity. Then the multistage time stepping scheme is formulated as

$$\begin{aligned}
\mathbf{w}^{(n+1,0)} &= \mathbf{w}^n \\
&\cdots \\
\mathbf{w}^{(n+1,k)} &= \mathbf{w}^n - \alpha_k \Delta t \left(C^{(k-1)} + \mathcal{D}^{(k-1)} \right) \\
&\cdots \\
\mathbf{w}^{n+1} &= \mathbf{w}^{(n+1,m)}
\end{aligned}$$

where the superscript k denotes the k-th stage, $\alpha_m = 1$, and

$$\begin{aligned}
C^{(0)} &= C(\mathbf{w}^n), \quad \mathcal{D}^{(0)} = \mathcal{D}(\mathbf{w}^n) \\
&\cdots \\
C^{(k)} &= C\left(\mathbf{w}^{(n+1,k)}\right) \\
\mathcal{D}^{(k)} &= \beta_k \mathcal{D}\left(\mathbf{w}^{(n+1,k)}\right) + (1-\beta_k)\mathcal{D}^{(k-1)}
\end{aligned}$$

The coefficients α_k are chosen to maximize the stability interval along the imaginary axis, and the coefficients β_k are chosen to increase the stability interval along the negative real axis.

A five-stage scheme with three evaluations of dissipation has been found to be particularly effective. Its coefficients are

$$\begin{array}{ll}
\alpha_1 = 1/4 & \beta_1 = 1 \\
\alpha_2 = 1/6 & \beta_2 = 0 \\
\alpha_3 = 3/8 & \beta_3 = 0.56 \\
\alpha_4 = 1/2 & \beta_4 = 0 \\
\alpha_5 = 1 & \beta_5 = 0.44
\end{array}$$

The actual time step Δt is limited by the Courant number (CFL), which states that the fastest waves in the system may not be allowed to propagate farther than the smallest grid spacing over the course of a time step. In this work, local time stepping is used such that regions of large grid spacing are permitted to have relatively larger time steps than regions of small grid spacing. Of course the system wave speeds vary locally and must be taken into account as well. The final local time step is thus computed as,

$$\Delta t^*{}_{ijk} = \frac{(CFL)\Lambda_{ijk}}{\lambda_{ijk}}$$

where λ_{ijk} is the sum of the spectral radii of both the convective and viscous flux Jacobian matrices in the x, y and z directions. In regions of small grid spacing and/or regions of high characteristic wave speeds, the time step will be smaller than elsewhere.

3.1.4 Residual Averaging

The allowable Courant number may be increased by smoothing the residuals at each stage using the following product form in three dimensions [18]

$$(1-\epsilon_\xi\delta_\xi^2)(1-\epsilon_\eta\delta_\eta^2)(1-\epsilon_\zeta\delta_\zeta^2)\bar{R}=R$$

where ϵ_ξ, ϵ_η and ϵ_ζ are smoothing coefficients and the $\delta^2_{\xi,\eta,\zeta}$ are central difference operators in computational coordinates. Each residual R_{ijk} is thus replaced by an average of itself and the neighboring residuals.

3.1.5 Multigrid Scheme

Very rapid convergence to a steady state is achieved with the aid of a multigrid procedure. The idea behind the multigrid strategy is to accelerate evolution of the system of equations on the fine grid by introducing auxiliary calculations on a series of coarser grids. The coarser grid calculations introduce larger scales and larger time steps with the result that low-frequency error components may be efficiently and rapidly damped out. Auxiliary grids are introduced by doubling the grid spacing, and values of the flow variables are transferred to a coarser grid by the rule

$$\mathbf{w}_{2h}^{(0)}=T_{2h,h}\mathbf{w}_h,$$

where the subscripts denote values of the grid spacing parameter (ie. h is the finest grid, $2h$, $4h$, ... are successively coarser grids) and $T_{2h,h}$ is a transfer operator from a fine grid to a coarse grid. The transfer operator picks flow variable data at alternate points to define coarser grid data as well as the coarser grid itself. A forcing term is then defined as

$$\mathbf{P}_{2h}=\sum R_h(\mathbf{w}_h)-R_{2h}(\mathbf{w}_{2h}^{(0)}),$$

where R is the residual of the difference scheme. To update the solution on the coarse grid, the multistage scheme is reformulated as

$$\begin{aligned}\mathbf{w}_{2h}^{(1)} &= \mathbf{w}_{2h}^{(0)} - \alpha_1\Delta t^*(R_{2h}^{(0)}+P_{2h})\\ &\cdots\\ \mathbf{w}_{2h}^{(q+1)} &= \mathbf{w}_{2h}^{(0)} - \alpha_q\Delta t^*(R_{2h}^{(q)}+P_{2h})\\ &\cdots\end{aligned}$$

where $R^{(q)}$ is the residual of the qth stage. In the first stage, the addition of P_{2h} cancels $R_{2h}(\mathbf{w}^{(0)})$ and replaces it by $\sum R_h(\mathbf{w}_h)$, with the result that the evolution on the coarse grid is driven by the residual on the fine grid. The result $\mathbf{w}_{2h}^{(m)}$ now provides the initial data for the next grid $\mathbf{w}_{4h}^{(0)}$ and so on. Once the last grid has has been reached, the accumulated correction must be passed back through successively finer grids. Assuming a three grid scheme, let $\mathbf{w}_{4h}^{(+)}$ represent the final value of $\mathbf{w}_{4h}$. Then the correction for the next finer grid will be

$$\mathbf{w}_{2h}^{(+)}=\mathbf{w}_{2h}^{(m)}+I_{2h,4h}(\mathbf{w}_{4h}^{(+)}-\mathbf{w}_{4h}^{(0)}),$$

where $I_{a,b}$ is an interpolation operator from the coarse grid to the next finer grid. The final result on the fine grid is obtained in the same manner:

$$\mathbf{w}_h^{(+)}=\mathbf{w}_h^{(m)}+I_{h,2h}(\mathbf{w}_{2h}^{(+)}-\mathbf{w}_{2h}^{(0)}).$$

The process may be performed on any number of successively coarser grids. The only restriction in the present work being use of a structured grid whereby elements of the coarsest grid do not overlap the ship hull. A 4-level "W-cycle" is used in the present work for each time step on the fine grid [18].

3.1.6 Grid Refinement

The multigrid acceleration procedure is embedded in a grid refinement procedure to further reduce the computer time required to achieve steady state solutions on finely resolved grids. In the grid refinement procedure the flow equations are solved on coarse grids in the early stages of the simulation. The coarse grids permit large time steps, and the flow field and the wave pattern evolve quite rapidly. When the wave pattern approaches a steady state, the grid is refined by doubling the number of grid points in all directions and the flow variables and free surface location are interpolated onto the new grid. Computations then continue using the finer grid with smaller time steps. The multigrid procedure is applied at all stages of the grid refinement to accelerate the calculations on each grid in the sequence, producing a composite "full multigrid" scheme which is extremely efficient.

3.2 Free Surface Solution

Both a kinematic and dynamic boundary condition must be imposed at the free surface. For the fully nonlinear condition, the free surface must move with the flow (ie. up or down corresponding to the wave height and location) and

the boundary conditions applied on the distorted free surface. Equation 3 can be cast in a form more amenable to numerical computations by introducing a curvilinear coordinate system that transforms the curved free surface $\beta(x,y)$ into computational coordinates $\beta(\xi,\eta)$. This results in the following transformed kinematic condition

$$\beta_{t^*} + \tilde{u}\beta_\xi + \tilde{v}\beta_\eta = w, \qquad (12)$$

where $\tilde{u}$ and $\tilde{v}$ are contravariant velocity components given by

$$\tilde{u} = u\xi_x + v\xi_y$$

$$\tilde{v} = u\eta_x + v\eta_y.$$

The free surface kinematic equation may now be expressed as

$$\frac{d\beta_{ij}}{dt^*} + Q_{ij}(\beta) = 0$$

where $Q_{ij}(\beta)$ consists of the collection of velocity and spacial gradient terms which result from the discretization of equation 12. Note that this is not the result of a volume integration and thus the volume (or actually area) term does not appear in the residual as in the FVM formulation. Throughout the interior of the (x,y) plane, all derivatives are computed using the second order centered difference stencil in computational coordinates ξ and η. On the boundaries a second order centered stencil is used along the boundary tangent and a first order one sided difference stencil is used in the boundary normal direction.

As was necessary in the FVM formulation for the bulk flow, background dissipation must be added to prevent decoupling of the solution. The method used to compute the dissipative terms borrows from a two dimensional FVM formulation and appears as follows:

$$D_{ij} = D_\xi + D_\eta$$

where

$$D_{\xi_{ij}} = d_{\xi_{i+1,j}} - d_{\xi_{i,j}}$$

and

$$d_{\xi_{i,j}} = \alpha\delta_\xi^2(\beta_{i+1,j} - \beta_{i,j}).$$

The expression for α may be written as

$$\alpha = \epsilon(|\tilde{u}_{i+1,j}| + |\tilde{u}_{i,j}|)J$$

where J is the sum of the cell Jacobians and ϵ is used to manually adjust the amount of dissipation. Hence the system of equations for the free surface is expressed as

$$\frac{d\beta_{ij}}{dt^*} + R_{ij}(\beta) = 0$$

where

$$R_{ij} = Q_{ij} - D_{ij}.$$

The same scheme used to integrate equation 11 is also used here. Once the free surface update is accomplished the pressure is adjusted on the free surface such that

$$\psi^{(n+1)} = \beta^{(n+1)}Fr^{-2}.$$

The free surface and the bulk flow solutions are coupled by first computing the bulk flow at each time step, and then using the bulk flow velocities to calculate the movement of the free surface. After the free surface is updated, its new values are used as a boundary condition for the pressure on the bulk flow for the next time step. The entire iterative process, in which both the bulk flow and the free surface are updated at each time step, is repeated until some measure of convergence is attained; usually steady state wave profile and wave resistance coefficient.

Since the free surface is a material surface, the flow must be tangent to it in the final steady state. During the iterations, however, the flow is allowed to *leak* through the surface as the solution evolves towards the steady state. This leakage, in effect, drives the evolution equation. Suppose that at some stage, the vertical velocity component w is positive (cf. equation 3 or 12). Provided that the other terms are small, this will force β^{n+1} to be greater than β^n. When the time step is complete, ψ is adjusted such that $\psi^{n+1} > \psi^n$. Since the free surface has moved farther away from the original undisturbed upstream elevation and the pressure correspondingly increased, the velocity component w (or better still $\mathbf{q}\cdot\mathbf{n}$ where $\mathbf{n} = \frac{\nabla F}{|\nabla F|}$ and $F = z - \beta(x,y)$) will then be reduced. This results in a smaller $\Delta\beta$ for the next time step. The same is true for negative vertical velocity, in which case there is mass leakage into the system rather than out. Only when steady state has been reached is the mass flux through the surface zero and tangency enforced. In fact, the residual flux leakage could be used in addition to drag components and pressure residuals as a measure of convergence to the steady state.

This method of updating the free surface works well for the Euler equations since tangency along the hull can be easily enforced. However, for the Navier-Stokes equations the no-slip boundary condition is inconsistent with the free surface boundary condition at the hull/waterline intersection. To circumvent this difficulty the

computed elevation for the second row of grid points away from the hull is extrapolated to the hull. Since the minimum spacing normal to the hull is small, the error due to this should be correspondingly small, comparable with other discretization errors. The treatment of this intersection for the Navier-Stokes calculations, should be the subject of future research to find the most accurate possible procedure.

4 Results

4.1 Computational Conditions

Figures 2 and 3 show portions of the fine grids used for the Navier-Stokes calculations. The number of grid points is 193, 65 and 49 in the x, y and z-directions respectively, and the $H-H$ type grid is used. Grid points are clustered near the bow and stern with a minimum spacing of 0.005 dimensionless units based on the hull length. The grid extends $\frac{1}{2}$ ship length upstream from the bow, $1\frac{1}{2}$ ship lengths downstream from the stern, $1\frac{1}{2}$ ship lengths to starboard, and 1 ship length down below the undisturbed free surface. The minimum spacing in the y-direction, normal to the hull surface, is 0.0001 for the Navier-Stokes computations and 0.0025 for the Euler computations. The resolution on the hull surface is 97 by 17 for the Wigley hull and 97 by 25 for the Series 60. Only the number of grid points in the y-direction is changed for the Euler calculations; rather than 65 the number is 49.

The following subsections present the computational results for the Wigley hull and the Series 60, $C_b = 0.6$ hull.

4.2 Wigley Hull

Figures 4 through 9 display computed and experimental results for the Wigley hull at Froude numbers 0.250 and 0.289. Both the Euler and the Navier-Stokes results for the waterline profile along the hull show good agreement with the experimental data [28]. Discrepancies are noted in the stern region where the Navier-Stokes model produces a slight flattening of the wave profile but correctly captures the aft-most waterline elevation, whereas the Euler model shows no tendency to flatten the wave profile but incorrectly predicts the aft-most waterline elevation. The computed wave drag (cf. fig. 5), obtained by integrating the longitudinal component of pressure on the wetted hull surface, shows favorable agreement with the experimentally determined value, $C_{w(exp)} = 0.821$. The experimental wave drag is inferred by subtracting an estimate of the friction drag from the total drag or by wave analysis. Note that the computed wave drag is evaluated after each multigrid cycle and hence the evolution of the drag is plotted vs. the steady state drag (marked by the x's) determined experimentally. The capital letters C, M and F refer to coarse, medium and fine grids respectively in the grid refinement procedure. The comparisons between computed overhead profiles show agreement between the two methods, except in the stern region and aft where viscous effects cause separation of the flow and a reduction in the amplitudes of the downstream waves (cf. fig. 6).

Essentially the same behavior is noted for the Fr = 0.289 case in the next set of figures. The waterline profile is predicted almost exactly for the Navier-Stokes simulation whereas the Euler case predicts a lower waterline level at the stern region. The computed values of the wave drag are in good agreement with the experimentally determined value $C_{w,exp} = 1.18$.

Figures 11 and 10 are included to show the computed velocity profile at the hull/waterline intersection. The prediction of separation is clearly evident in the stern region of the hull.

4.3 Series 60, $C_b = 0.6$ Hull

In contrast to the Wigley hull, which is an idealized shape, the Series 60 hull is a practical geometry for an actual ship hull. The only major difference in the method of computing the flow about this hull and the Wigley model is the effort required to maintain the proper hull shape as the grid is distorted by the moving free surface. To accomplish this, a grid is produced for the entire hull, both above and below the undisturbed free surface. Spline coefficients are then determined for the entire grid and stored. A new grid is then produced with the uppermost plane of points residing in the plane of the undisturbed waterline at $z = 0$. With the stored spline data the grid is now easily updated as the free surface evolves by redistributing points at intervals of equally spaced arc length. It was found that this method prevents the grid lines from crossing at the close tolerances required for the viscous computations.

The waterline contours shown in figure 12 are in reasonably good agreement for both the Euler and Navier-Stokes simulations. Except for the

bow region, it appears that the Euler method does an equally good job, if not better, than the Navier-Stokes method. There is some discrepancy amidship in the Navier-Stokes computation which is possibly due to the method used to update points on the hull/waterline intersection set of points. However, as in the Wigley cases, the drag calculation is in good agreement with experiment ($C_{w,exp} = 2.6$) [29] and the overhead profiles show good agreement with each other.

5 Conclusions

The objective of the present work was to develop an efficient method to compute Euler and Navier-Stokes solutions for the nonlinear ship wave problem. The results for the Wigley hull and Series 60 hull suggest that the objective has been reached and the resulting computer code has been validated, at least for the range of test cases examined. The wave elevations predicted by the numerical simulations are in excellent agreement with the experimental measurements. In addition, the computed wave drag is in good agreement with the wave drag inferred from the experiments.

The Euler method, which requires significantly less computational resources than the Navier-Stokes method, produces results that appear to be within a reasonable degree of accuracy for engineering design work. As the present method is refined and improved, and applied to other geometries (such as submarines, sailing yachts and more practical stern flows), it is planned to continue the comparison between the two methods in order to establish the conditions under which the Euler method can be expected to give accurate results.

The computational times for the simulations are approximately 10 and 12 hours for the Euler calculations on the Wigley and Series 60 hulls, respectively, and approximately 18 hours for the Navier-Stokes calculations for both hulls. The Euler simulations consist of 100 steps on a $49 \times 13 \times 13$ grid, 200 steps on a $97 \times 25 \times 25$ grid and 200 steps on a $193 \times 49 \times 49$ grid. The Navier-Stokes simulations consist of 100 steps on a $49 \times 17 \times 13$ grid, 200 steps on a $97 \times 33 \times 25$ grid and 200 steps on a $193 \times 65 \times 49$ grid. These times were recorded in calculations using a single processor Convex 3400 computer with 64-bit arithmetic. For the given resolution they appear to represent about a ten-fold decrease in the CPU times reported in the earlier literature, which have usually been presented for coarser grids. The CPU time required for the free surface update and regriding procedures is approximately seven percent that required for the bulk flow calculations.

Acknowledgment

The authors gratefully appreciate the contribution of James Reuther (NASA-Ames) for his time and effort spent helping construct the grids used for the Series 60 hull. We would also like to thank Dr. Takanori Hino for the many helpful discussions concerning this work during his research appointment at Princeton. Our work has benefited greatly from the support of the Office of Naval Research through Grant N00014-93-I-0079, under the supervision of Dr. E.P. Rood.

References

[1] Toda,Y., Stern,F., and Longo,J., "Mean-Flow Measurements in the Boundary Layer and Wake and Wave Field of a Series 60 $C_B = 0.6$ Ship Model–Part1: Froude Numbers 0.16 and 0.316," *Journal of Ship Research,* v. 36, n. 4, pp. 360-377, 1992.

[2] Longo,J., Stern,F., and Toda,Y., "Mean-Flow Measurements in the Boundary Layer and Wake and Wave Field of a Series 60 $C_B = 0.6$ Ship Model–Part2: Effects on Near-Field Wave Patterns and Comparisons with Inviscid Theory", *Journal of Ship Research,* v. 37, n. 1, pp. 16-24, 1993.

[3] Hino,T., "Computation of Free Surface Flow Around an Advancing Ship by the Navier-Stokes Equations", *Proceedings, Fifth International Conference on Numerical Ship Hydrodynamics,* pp. 103-117, 1989.

[4] Miyata,H., Toru,S., and Baba,N., "Difference Solution of a Viscous Flow with Free-Surface Wave about an Advancing Ship", *Journal of Computational Physics,* v. 72, pp. 393-421, 1987.

[5] Miyata,H., Zhu,M., and Wantanabe,O., "Numerical Study on a Viscous Flow with Free-Surface Waves About a Ship in Steady Straight Course by a Finite-Volume Method", *Journal of Ship Research,* v. 36, n. 4, pp. 332-345, 1992.

[6] Tahara,Y., Stern,F., and Rosen,B., "An Interactive Approach for Calculating Ship Boundary

Layers and Wakes for Nonzero Froude Number", *Journal of Computational Physics,* v. 98, pp. 33-53, 1992.

[7] Chen,H.C., Patel,V.C., and Ju,S., "Solution of Reynolds-Averaged Navier-Stokes Equations for Three-Dimensional Incompressible Flows", *Journal of Computational Physics,* v. 88, pp. 305-336, 1990.

[8] Rosen,B.S., Laiosa,J.P., Davis,W.H., and Stavetski,D., "SPLASH Free-Surface Flow Code Methodology for Hydrodynamic Design and Analysis of IACC Yachts", *The Eleventh Chesapeake Sailing Yacht Symposium,* Annapolis, MD, 1993.

[9] Chorin,A., "A Numerical Method for Solving Incompressible Viscous Flow Problems", *Journal of Computational Physics,* v. 2, pp. 12-26, 1967.

[10] Rizzi,A., and Eriksson,L., "Computation of Inviscid Incompressible Flow with Rotation", *Journal of Fluid Mechanics,* v. 153, pp. 275-312, 1985.

[11] Dreyer,J., "Finite Volume Solutions to the Unsteady Incompressible Euler Equations on Unstructured Triangular Meshes", M.S. Thesis, MAE Dept., Princeton University, 1990.

[12] Kodama,Y., "Grid Generation and Flow Computation for Practical Ship Hull Forms and Propellers Using the Geometrical Method and the IAF Scheme", *Proceedings, Fifth International Conference on Numerical Ship Hydrodynamics,* pp. 71-85, 1989.

[13] Turkel,E., "Preconditioned Methods for Solving the Incompressible and Low Speed Compressible Equations", ICASE Report 86-14, 1986.

[14] Jameson,A., Baker,T., and Weatherill,N., "Calculation of Inviscid Transonic Flow Over a Complete Aircraft", *AIAA Paper 86-0103, AIAA 24th Aerospace Sciences Meeting,* Reno, NV, January 1986.

[15] Jameson,A., "Computational Aerodynamics for Aircraft Design", *Science,* v. 245, pp. 361-371, 1989.

[16] Jameson,A., "Solution of the Euler Equations for Two Dimensional Transonic Flow by a Multigrid Method", *Applied Math. and Computation,* v. 13, pp. 327-356, 1983.

[17] Jameson, A., "Computational Transonics", *Comm. Pure Appl. Math.,* v. 41, pp. 507-549, 1988.

[18] Jameson,A., "A Vertex Based Multigrid Algorithm For Three Dimensional Compressible Flow Calculations", *ASME Symposium on Numerical Methods for Compressible Flows,* Annaheim, December 1986.

[19] Farmer,J., "A Finite Volume Multigrid Solution to the Three Dimensional Nonlinear Ship Wave Problem", Ph.D. Thesis, MAE 1949-T, Princeton University, January 1993.

[20] Farmer,J., Martinelli,L., and Jameson,A., "A Fast Multigrid Method for Solving Incompressible Hydrodynamic Problems with Free Surfaces", Accepted for publication in the AIAA Journal, 1993.

[21] Orlanski,I., "A Simple Boundary Condition for Unbounded Hyperbolic Flows", *Journal of Computational Physics,* v. 21, 1976.

[22] Baldwin,B.S., and Lomax,H., "Thin Layer Approximation and Algebraic Model for Separated Turbulent Flows", *AIAA Paper 78-257, AIAA 16th Aerospace Sciences Meeting,* Reno, NV, January 1978.

[23] Yang,C-I., Hartwich,P-M., and Sundaram,P., "Numerical Simulation of Three-Dimensional Viscous Flow around a Submersible Body", *Proceedings, Fifth International Conference on Numerical Ship Hydrodynamics,* pp. 59-69, 1989.

[24] Martinelli,L., "Calculations of Viscous Flows with a Multigrid Method", Ph.D. Thesis, MAE 1754-T, Princeton University, 1987.

[25] Martinelli,L. and Jameson,A., "Validation of a Multigrid Method for the Reynolds Averaged Equations", *AIAA Paper 88-0414, AIAA 26st Aerospace Sciences Meeting,* Reno, NV, January 1988.

[26] Liu,F. and Jameson,A., "Multigrid Navier-Stokes Calculations For Three-Dimensional Cascades", *AIAA Paper 92-0190, AIAA 30th Aerospace Sciences Meeting,* Reno, NV, January 1990.

[27] Martinelli,L., Jameson,A., and Malfa,E., "Numerical Simulation of Three-Dimensional Vortex Flows Over Delta Wing Configurations", *Lecture Notes in Physics, Volume 414. Thirteenth International Conference on Numerical Methods in Fluid Dynamics,.* M. Napolitano and F. Sabetta (Eds.), Rome, Italy, 1992.

[28] "Cooperative Experiments on Wigley Parabolic Models in Japan", *17th ITTC Resistance Committee Report,* 2nd ed., 1983.

[29] Toda,Y., Stern,F., and Longo,J., "Mean-Flow Measurements in the Boundary Layer and Wake and Wave Field of a Series 60 $C_B = 0.6$ Ship Model for Froude Numbers .16 and .316", IIHR Report No. 352, Iowa Institute of Hydraulic Research, The University of Iowa, Iowa City, Iowa, 1991.

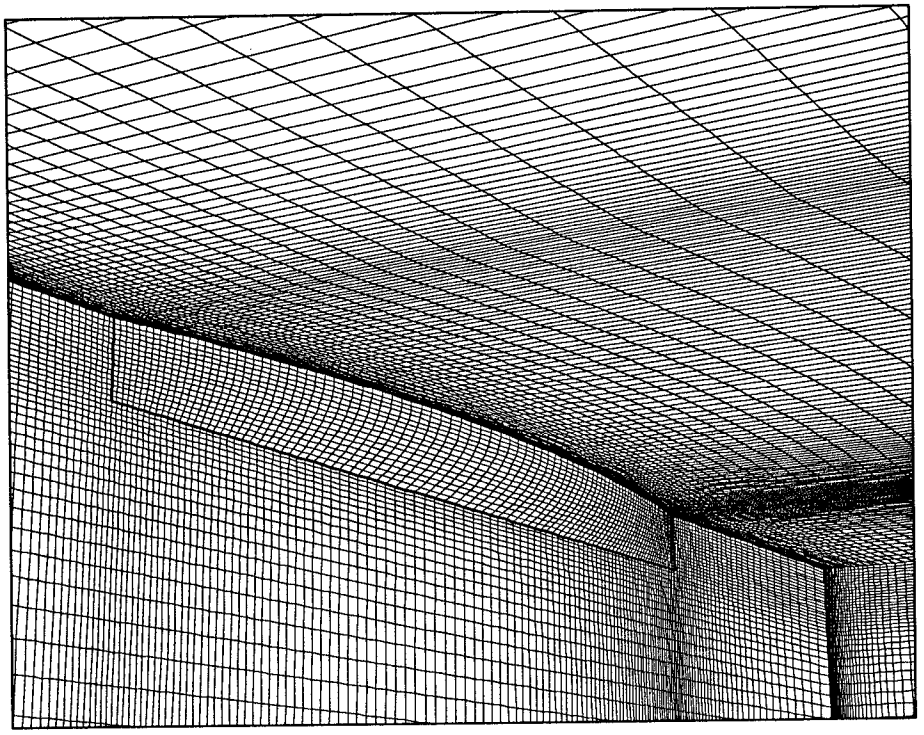

Figure 2: Fine Grid for Wigley Hull Navier-Stokes Computations ($193 \times 65 \times 49$)

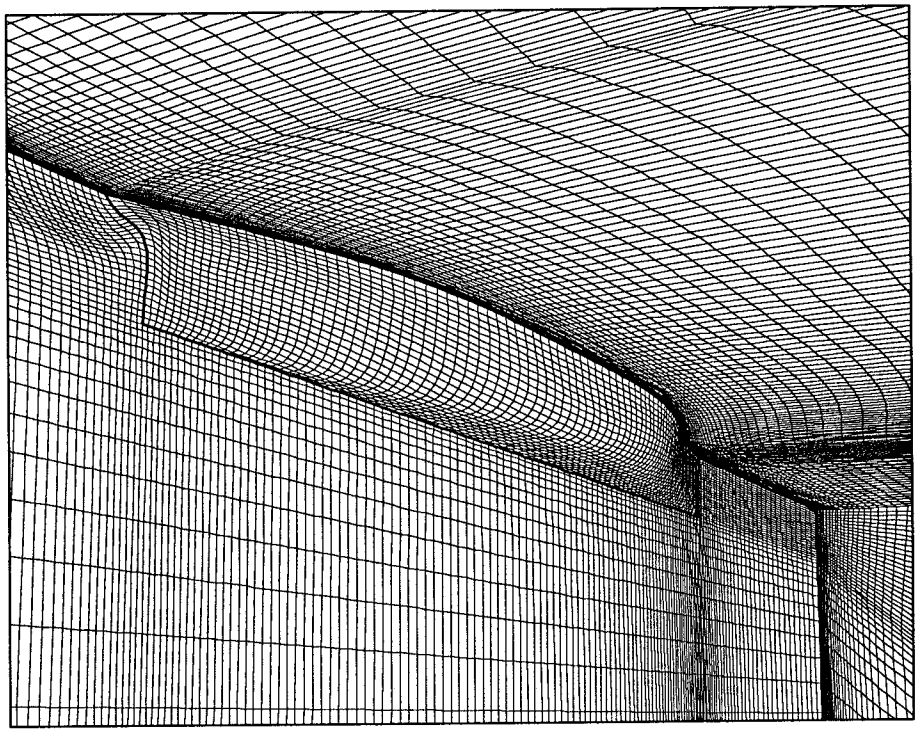

Figure 3: Fine Grid for Series 60, $C_b = 0.6$ Navier-Stokes Computations ($193 \times 65 \times 49$)

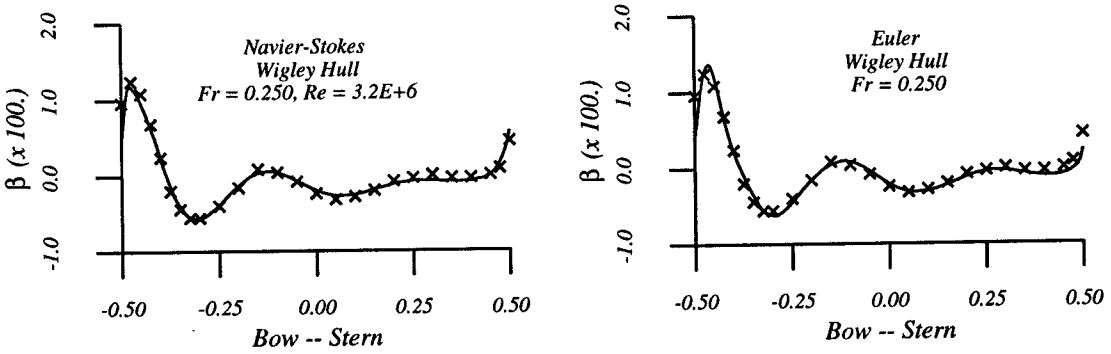

Figure 4: Computed vs. Experimental Wave Elevation

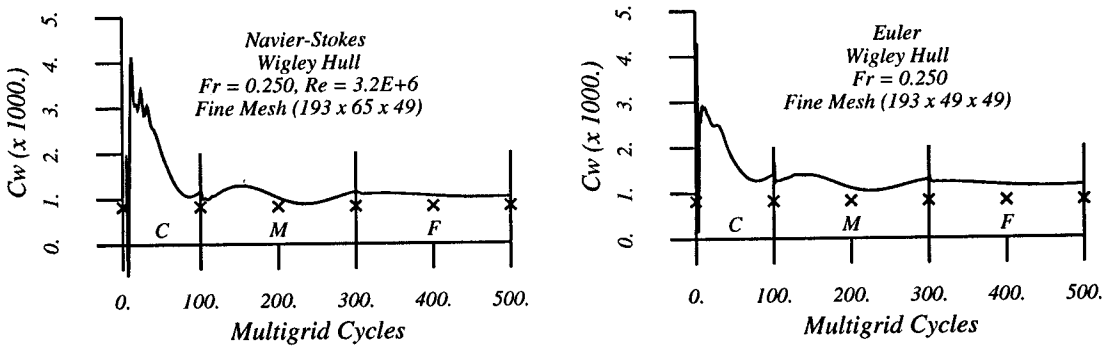

Figure 5: Computed vs. Experimental Wave Drag
C = Coarse Mesh, M = Medium Mesh, F = Fine Mesh

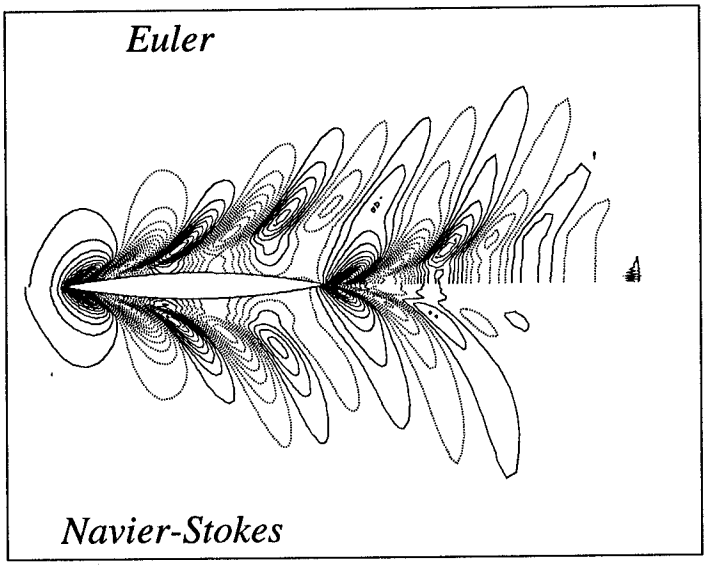

Figure 6: Comparison of Computed Overhead Wave Profiles, Wigley Hull, Fr = 0.250

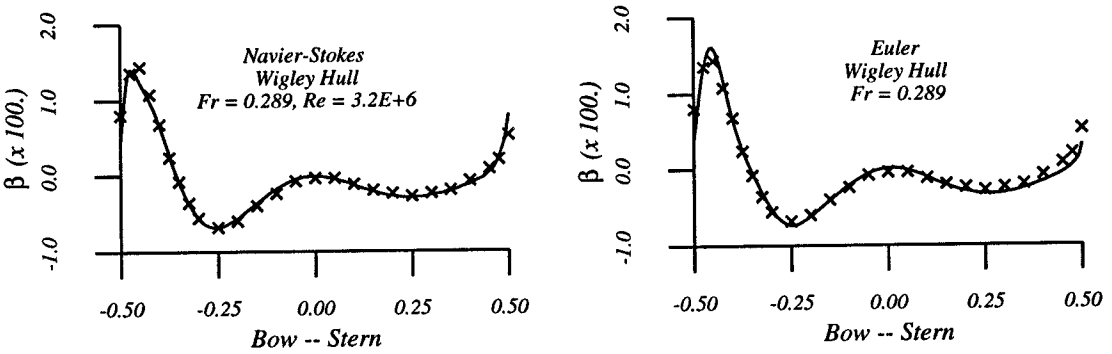

Figure 7: Computed vs. Experimental Wave Elevation

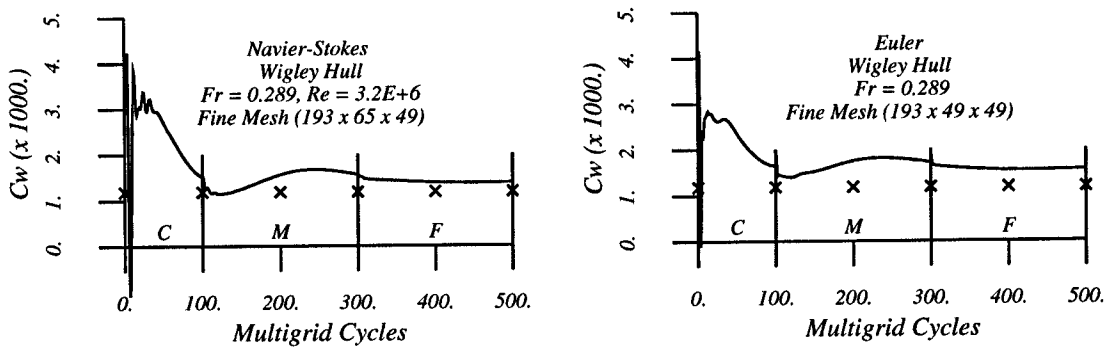

Figure 8: Computed vs. Experimental Wave Drag
C = Coarse Mesh, M = Medium Mesh, F = Fine Mesh

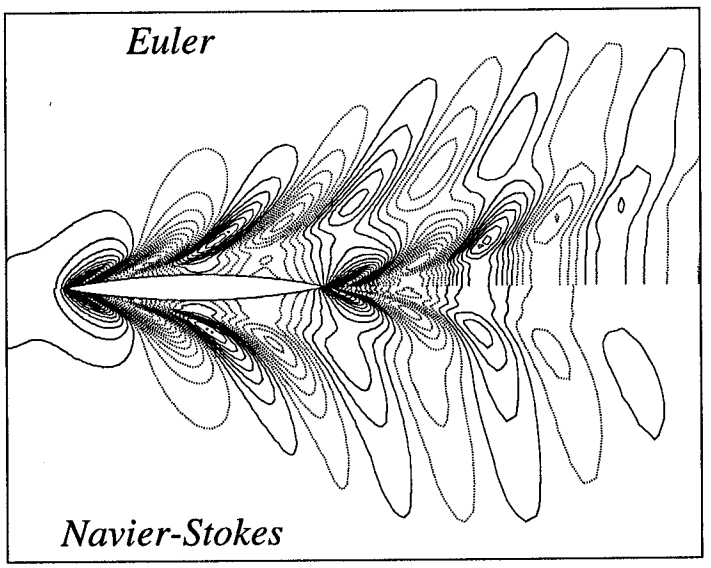

Figure 9: Comparison of Computed Overhead Wave Profiles, Wigley Hull, Fr = 0.289

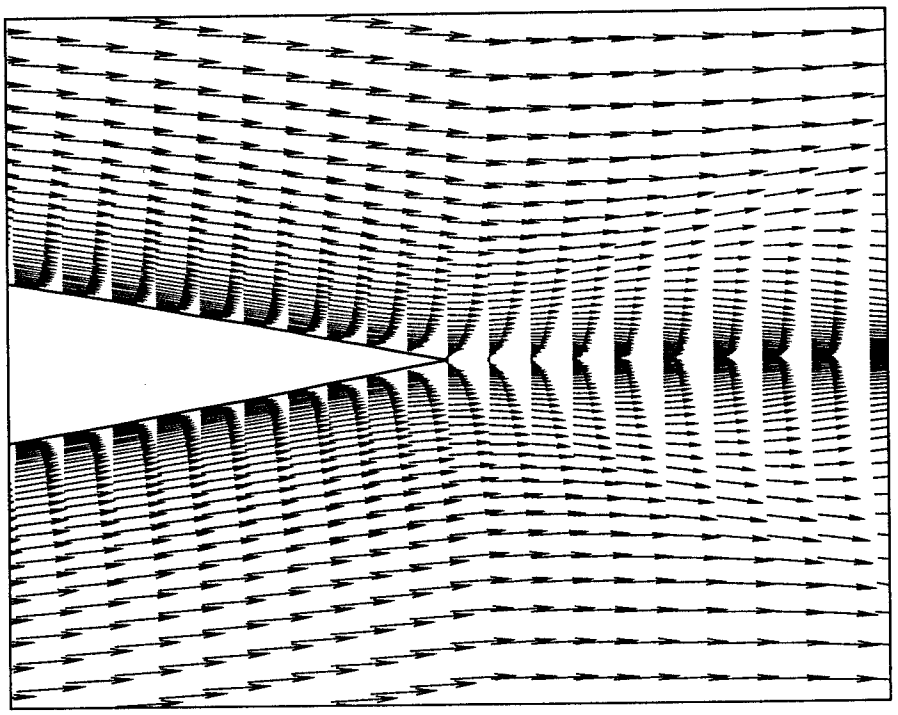

Figure 10: Velocity Vectors, Wigley Hull Stern Region, Fr = 0.289, Re = 3.2E+06

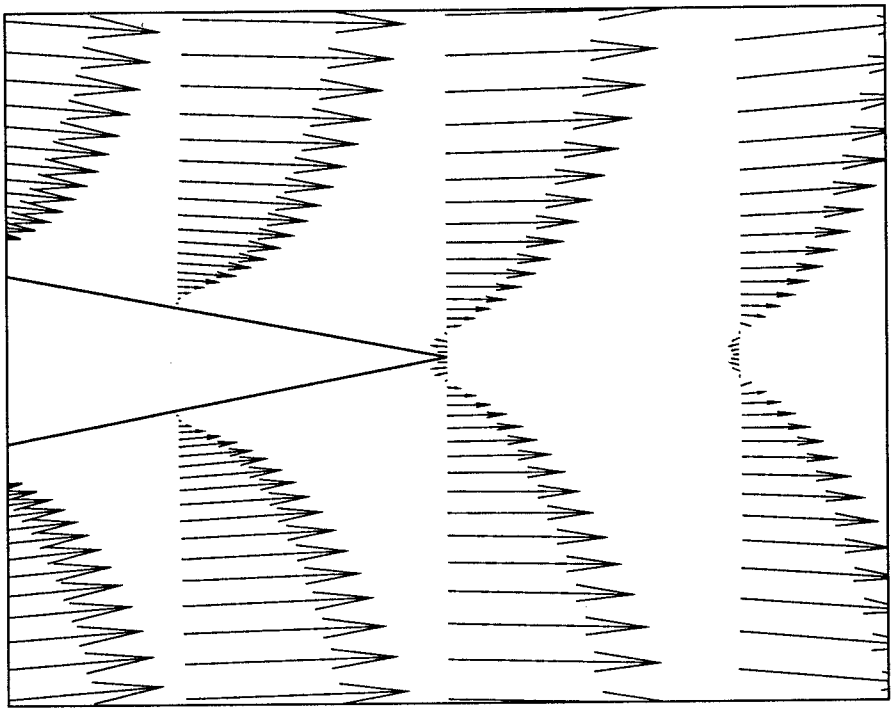

Figure 11: Velocity Vectors, Wigley Hull Stern Region, Fr = 0.289, Re = 3.2E+06
(close up view)

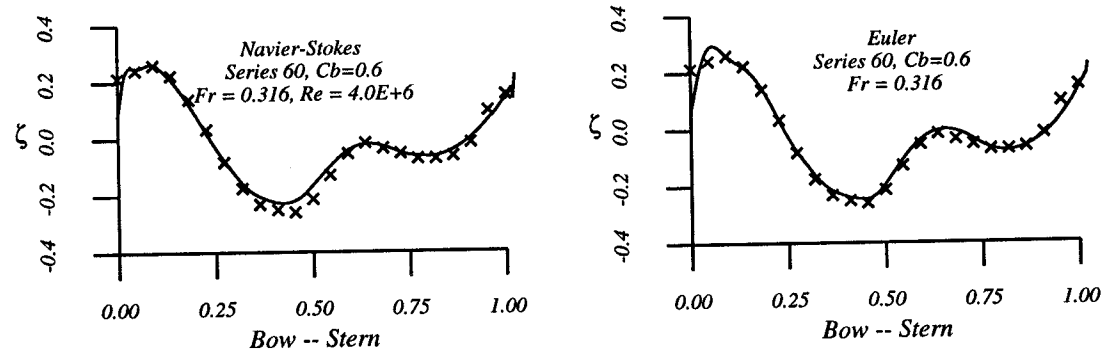

Figure 12: Computed vs. Experimental Wave Elevation, ($\zeta = 2\beta Fr^{-2}$)

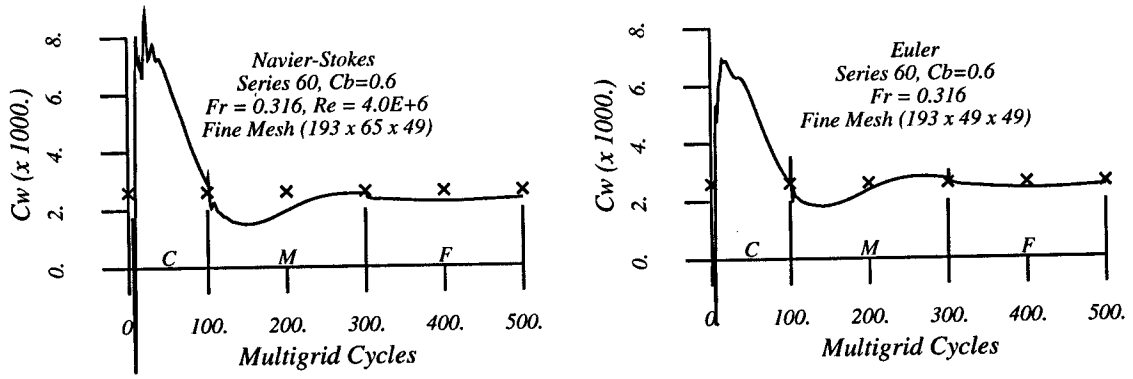

Figure 13: Computed vs. Experimental Wave Drag
C = Coarse Mesh, M = Medium Mesh, F = Fine Mesh

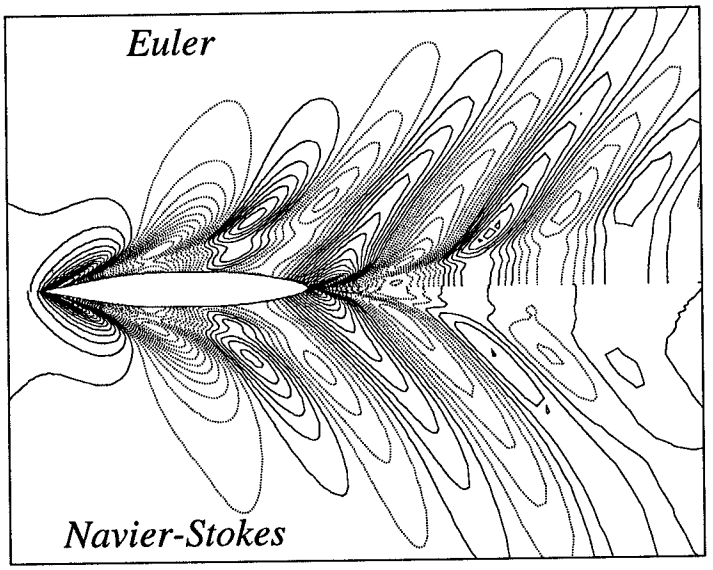

Figure 14: Comparison of Computed Overhead Wave Profiles, Series 60, $C_b = 0.6$, Fr = 0.316